Nanoscale Advances

ROYAL SOCIETY OF CHEMISTRY

PAPER

View Article Online
View Journal | View Issue

Cite this: *Nanoscale Adv.*, 2022, **4**, 782

Controllable synthesis of variable-sized magnetic nanocrystals self-assembled into porous nanostructures for enhanced cancer chemo-ferroptosis therapy and MR imaging†

Jianxiang Xu,‡[a] Hanyuan Zhang,‡[b] Yifei Zhang,[c] Xu Zhang,[a] Teng Wang,[a] Shi Hong,[a] Wenmei Wei,[a] Tingting Zhao *[a] and Weijun Fang *[a]

Magnetic-based nanomaterials are promising for cancer diagnosis and treatment. Herein, we develop a self-assembled approach for the preparation of a porous magnetic nanosystem, DOX/Mn(0.25)-Fe_3O_4-III NPs, which can simultaneously achieve chemotherapy, ferroptosis therapy and MRI to improve the therapeutic efficacy. By tuning its porous structures, whole particle sizes and compositions, this nanosystem possesses both a high drug loading capacity and excellent Fenton reaction activity. Owing to the synergetic catalysis effect of iron and manganese ions, the Fenton catalytic activity of Mn(0.25)-Fe_3O_4-III NPs ($K_{cat} = 1.2209 \times 10^{-2}$ min^{-1}) was six times higher than that of pure porous Fe_3O_4 NPs ($K_{cat} = 1.9476 \times 10^{-3}$ min^{-1}), making them greatly advantageous in ferroptosis-inducing cancer therapy. Moreover, we found out that these Mn(0.25)-Fe_3O_4-III NPs show a pH-dependent Fenton reaction activity. At acidic tumorous pH, this nanosystem could catalyze H_2O_2 to produce the cytotoxic $^{\bullet}OH$ to kill cancer cells, while in neutral physiological conditions it decomposed H_2O_2 into biosafe species (H_2O and O_2). *In vivo* studies demonstrated that DOX/Mn(0.25)-Fe_3O_4-III NPs exhibited a significant synergistic anticancer effect of combining chemotherapy and ferroptosis therapy and effective T_2-weighted MRI with minimal side effects. Therefore, this porous magnetic nanoplatform has a great potential for combined diagnosis and therapy in future clinical applications.

Received 24th October 2021
Accepted 21st December 2021

DOI: 10.1039/d1na00767j

rsc.li/nanoscale-advances

1. Introduction

Superparamagnetic iron oxide nanoparticles (Fe_3O_4 NPs) are widely used in numerous medical fields, including drug delivery, magnetic resonance imaging (MRI), hyperthermia, magnetic targeting and magnetofection.[1–3] The choice of Fe_3O_4 NPs can be related to their several advantages over other types of nanomaterials. First, they, acting as drug nanovehicles, can be easily guided into the tumor site by an external magnetic force, which results in improving the efficiency of the tumor treatment. Second, they can be used as contrast agents in MRI without tedious functionalized procedures. Finally, these Fe_3O_4 NPs have high biocompatibility and have been approved by the FDA. Currently, there are several types of iron oxide NPs in the market as contrast agents for clinical MRI (Endorem®/Feridex I.V.®, Abdoscan®, Lumirem®/GastroMARK®).[4,5]

A porous structure is one of the important characteristics of a smart drug-delivery nanocarrier. Porosity provides nanocarriers with a large inner surface area, which can achieve a high drug loading capacity and controllable drug release, as drug adsorption/desorption is a surface-based phenomenon. To acquire this porosity, iron oxide nanoparticles integrated with porous materials have been developed.[6–19] These magnetic nanocomposites show excellent anticancer properties and open up a wide field of possible applications in cancer theranostics. However, most reported iron oxide-based porous nanocomposites are involved in multi-step and time-consuming synthetic procedures, and the risk of introducing new toxic substances. Therefore, the direct and effective synthesis of pure porous Fe_3O_4 NPs is highly demanded.

Ferroptosis is a non-apoptotic form of regulated cell death, which depends on the concentration of intracellular iron ions and reactive oxygen species (ROS).[19–21] The mechanism of ferroptosis is regulated by a series of complex gene expression and signal transduction.[22,23] Up to now, some regulation mechanisms and signaling pathways of ferroptosis have been clarified. In particular, the iron-catalyzed ROS production pathway

[a]*School of Basic Medical Sciences, Anhui Medical University, Hefei, 230032, Anhui, China. E-mail: fangweijun@ahmu.edu.cn; wjfang812163.com*

[b]*Department of Orthopedics, Department of Sports Medicine and Arthroscopic Surgery, The First Affiliated Hospital of Anhui Medical University, Hefei, 230022, China*

[c]*Department of Orthopaedics, The Third Affiliated Hospital of Anhui Medical University, Hefei, 230061, China*

† Electronic supplementary information (ESI) available. See DOI: 10.1039/d1na00767j

‡ These authors contributed equally to this work.

(called as Fenton reaction) has been widely accepted.[24–26] Using the key role of iron in ferroptosis, various iron-based nanostructures have been developed for ferroptosis-inducing cancer therapy,[27–29] such as Fe_3O_4,[30–34] γ-Fe_2O_3,[35] FePt,[36] Fe^{3+}/polymer,[37–41] Iron-MOF,[42,43] FeS_2-PEG[44] and oxide iron-based nanocomposites.[45–47] More importantly, Mn(0.25)-Fe_3O_4-III NPs act as Fenton agents, which show extremely high Fenton reaction activity compared with numerous reported iron-based nanoparticles. The drug delivery properties, Fenton catalytic activities, MR imaging abilities, chemotherapy and ferroptosis therapy of DOX/Mn(0.25)-Fe_3O_4-III NPs were systematically studied. Finally, the Hematoxylin and Eosin (H&E) staining of main organs, including heart, liver, spleen, lungs and kidney, was carried out to investigate the *in vivo* biosafety of our nanosystem.

2. Results and discussion

2.1 Preparation and characterization of the porous Mn-doped Fe_3O_4 NPs

The design for the fabrication of porous Mn-doped Fe_3O_4 NPs is illustrated in Fig. 1A. The particle size and porous structure of the Mn-doped Fe_3O_4 NPs were modulated by controlling the amount of water. A decrease in the whole particle size and increase in the nanocrystal size were observed by both transmission electron microscopy (TEM) and scanning electron microscopy (SEM) when the amount of water increased. From Fig. 1B–I, as the water increased from 0, 170, 304 to 800 μL, the average particle size of the whole magnetic nanospheres changed to ~206 nm (Fig. 1B and F), ~164 nm (Fig. 1C and G), ~124 nm (Fig. 1D and H) and ~26 nm (Fig. 1E and I). For convenience, we labeled these samples as Mn(0.25)-Fe_3O_4-I NPs, Mn(0.25)-Fe_3O_4-II NPs, Mn(0.25)-Fe_3O_4-III NPs and Mn(0.25)-Fe_3O_4-IV NPs, respectively. The average nanocrystal size calculated from the strongest peak (311) (Fig. 1J) using the Debye–Scherrer's formula are ~8.9, 13.7, 17.7 nm and 26 nm for the as-synthesized Mn(0.25)-Fe_3O_4-I NPs, Mn(0.25)-Fe_3O_4-II NPs, Mn(0.25)-Fe_3O_4-III NPs and Mn(0.25)-Fe_3O_4-IV NPs, respectively, which were in good agreement with the magnification TEM images (Fig. 1F–I, inset).

In our reaction system, water plays a very important role in the formation of the Mn-doped Fe_3O_4 nanocrystals, which could regulate the size of the nanocrystals from ~8.9 nm to ~26 nm. As a result, the smaller size of nanocrystals can self-assemble into porous nanospheres, whereas when the size of nanocrystals reaches ~26 nm, they lose the ability to self-assemble into porous nanostructures (Fig. 1E and I). From the XRD analysis (Fig. 1J), all the detectable diffraction peaks can be indexed to a spinel cubic-phase Fe_3O_4 (JCPDS card no. 19-0629). No other peaks were observed, indicating the high purity of the product.

In Fig. 1K, the room-temperature magnetic hysteresis curves of these magnetic nanospheres exhibited no coercivity, and they were superparamagnetic at room temperature. Interestingly, the Mn(0.25)-Fe_3O_4-III NPs showed the highest saturation magnetization (M_s) with a value of 74.3 emu g^{-1} compared to Mn(0.25)-Fe_3O_4-I NPs with 54.5 emu g^{-1}, Mn(0.25)-Fe_3O_4-II NPs with 68.9 emu g^{-1} and Mn(0.25)-Fe_3O_4-IV NPs with 66.9 emu g^{-1}, indicating that the Mn(0.25)-Fe_3O_4-III NPs can sever as an excellent T_2-weighted MRI contrast agent since the contrast enhancement effects are directly related to the M_s value of the nanoparticles.[48–50]

The nitrogen adsorption/desorption isotherms demonstrated that Mn(0.25)-Fe_3O_4-III NPs had a well-developed mesoporous structure (Fig. 1L). The BET surface area, Barrett–Joyner–Halenda (BJH) pore size and total pore volume were 50.8 m^2 g^{-1}, 10.0 nm and 0.069 cm^3 g^{-1}, respectively. In addition, the elemental maps of different elements in Mn(0.25)-Fe_3O_4-III NPs were also done and the results are presented in Fig. S1†. As seen, the Fe, Mn and O elements are uniformly dispersed in the whole nanospheres. Their chemical compositions were further identified as $(Mn_{0.25}Fe_{0.75})Fe_2O_4$ by inductively coupled plasma-atomic emission spectrophotometry (ICP-AES).

2.2 *In vitro* drug loading and release behaviors of Mn(0.25)-Fe_3O_4-III NPs

The unique large pore structure (~10 nm in diameter) endows the Mn(0.25)-Fe_3O_4-III NPs with great potential applications in drug delivery. To evaluate their capacity as a drug delivery vehicle, DOX was chosen as a model drug and loaded into Mn(0.25)-Fe_3O_4-III NPs to prepare DOX-loaded Mn(0.25)-Fe_3O_4-III NPs (DOX/Mn(0.25)-Fe_3O_4-III NPs, Fig. 2A). Fig. 2B showed the color change of the DOX solution before and after incubation with Mn(0.25)-Fe_3O_4-III NPs. The color of the DOX solution changed from the red to colorless, confirming the complete loading of DOX into the Mn(0.25)-Fe_3O_4-III NPs. The loading amount of DOX in Mn(0.25)-Fe_3O_4-III NPs was about 4.5% (w/w) calculated from UV-vis absorption spectra (Fig. 2C). This high drug loading capacity was attributed to the large pore size and the coordination bonds between the amino groups in DOX molecules and iron ions on the Mn(0.25)-Fe_3O_4-III NPs' surface.

Fig. 2D shows the DOX release behavior of DOX/Mn(0.25)-Fe_3O_4-III NPs in PBS buffers at different pH values. It can be seen that the drug release rate of DOX/Mn(0.25)-Fe_3O_4-III NPs was slightly pH-dependent and increased with the decrease in pH. The cumulative release amount of DOX could reach up to 53% after 24 h at pH 6.0, slightly higher than that at pH 7.4, which was 48%.

2.3 *In vitro* catalytic activities of Mn(0.25)-Fe_3O_4-III NPs

Ferroptosis *via* the production of ROS has attracted great concern for cancer therapy. Up to now, some regulation mechanisms and signaling pathways of ferroptosis have been clarified. In particular, the iron-catalyzed ROS production pathway (called as Fenton reaction) has been widely accepted and is described in Fig. S2.†[27,51–54] Based on the Fenton reaction mechanism, iron oxide nanoparticles are preferred to catalyze H_2O_2 to produce hydroxyl radicals (˙OH) exhibiting peroxidase-like activities because they are able to release as iron ions (Fe^{2+}/Fe^{3+}) in the acidic environments (*e.g.*, endosomes and lysosomes). To check the peroxidase-like activities of Mn(0.25)-Fe_3O_4-III NPs, the colorless 3,3′,5,5′-tetramethyl-benzidine (TMB) was applied to detect the production of radicals. The

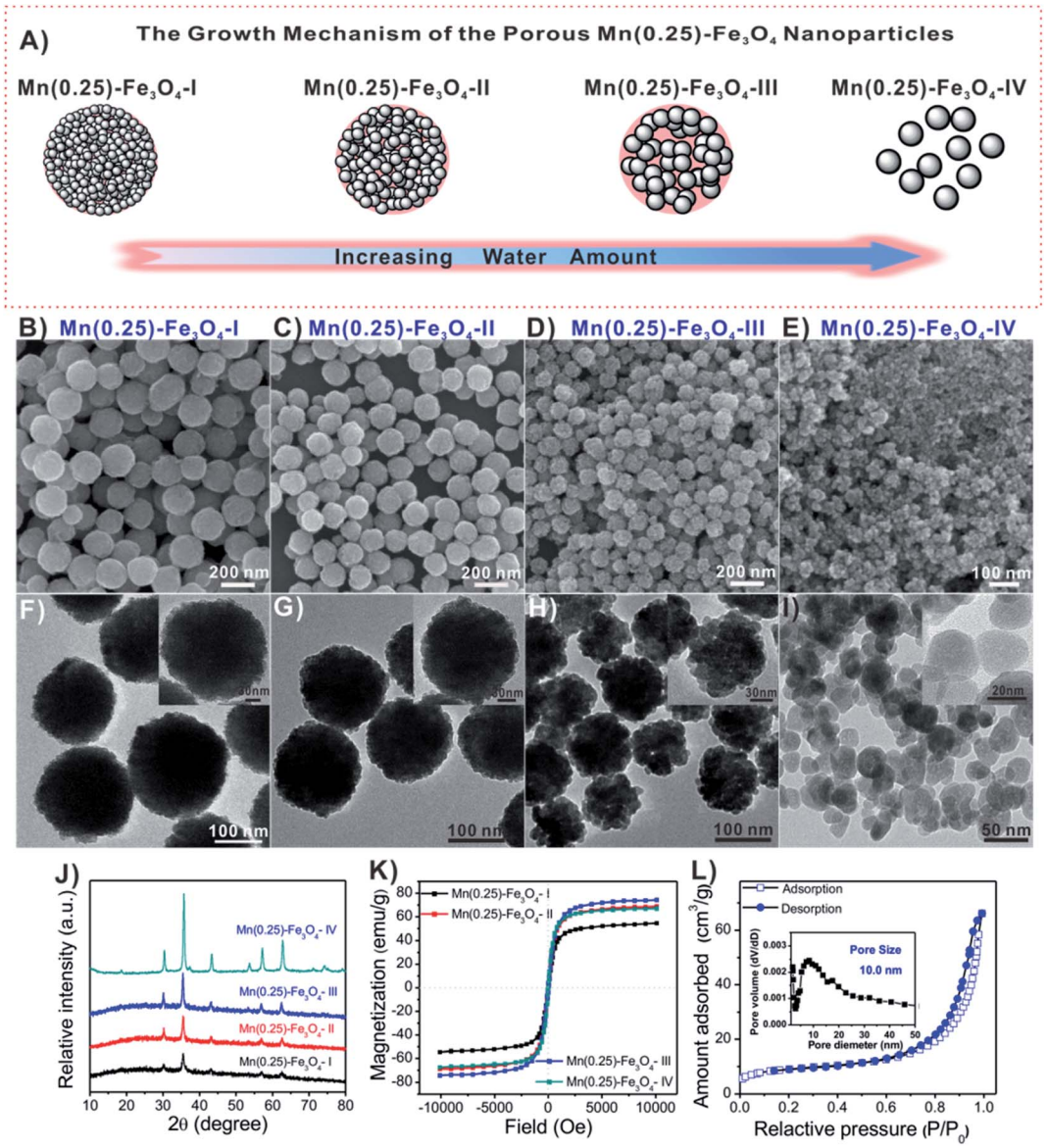

Fig. 1 (A) Schematic of the synthesis of porous Mn-doped Fe_3O_4 NPs. (B)–(E) SEM images and (F)–(I) TEM images of Mn(0.25)-Fe_3O_4-I NPs, Mn(0.25)-Fe_3O_4-II NPs, Mn(0.25)-Fe_3O_4-III NPs and Mn(0.25)-Fe_3O_4-IV NPs. Inset: images of single nanoparticles. (J) XRD patterns and (K) magnetization curves of Mn(0.25)-Fe_3O_4-I NPs, Mn(0.25)-Fe_3O_4-II NPs, Mn(0.25)-Fe_3O_4-III NPs and Mn(0.25)-Fe_3O_4-IV NPs. (L) N2 adsorption–desorption isotherms and pore size distributions (inset) of porous Mn(0.25)-Fe_3O_4-III NPs.

generation of $^{\bullet}OH$ from the Fenton reaction could oxidize TMB to form blue-colored TMB (oxTMB) with a maximum absorbance at 650 nm (Fig. 3A). As depicted in the UV-vis absorption spectra, there were nearly no absorbance at 650 nm in the H_2O_2 and H_2O_2/TMB solutions. However, an apparently blue-colored solution (Fig. 3B, inset) and high absorbance at 650 nm can be obtained after the addition of Mn(0.25)-Fe_3O_4-III NPs into the H_2O_2–TMB solution (pH = 4.8), which proves the production of $^{\bullet}OH$ by Mn(0.25)-Fe_3O_4-III NPs and H_2O_2 under an acidic condition. In addition, the time-dependent absorbance changes upon the addition of H_2O_2 were recorded in time-scan mode at 650 nm, and the initial velocity increased with the increase in the concentrations of H_2O_2 from 40 to 100 mM (Fig. 3C).

Interestingly, we find out that Mn(0.25)-Fe_3O_4-III NPs exhibit pH-dependent peroxidase-like and catalase-like activities. As mentioned above, Mn(0.25)-Fe_3O_4-III NPs exhibited peroxidase-like activities under the acidic conditions and could catalyze H_2O_2 to produce hydroxyl radicals. However, no hydroxyl radicals were detected in the neutral PBS solution (pH = 7.4, Fig. 3E). Instead, they decomposed H_2O_2 into water and oxygen in neutral conditions through catalase-like activities, as measured by a dissolved oxygen meter (Fig. 3F). Oxygen gas bubbles were observed after Mn(0.25)-Fe_3O_4-III NPs were added into the H_2O_2 solution. By increasing the concentrations of H_2O_2, more and more bubbles continued to form in the tubes (Fig. 3G). The generation of oxygen gas strongly supports

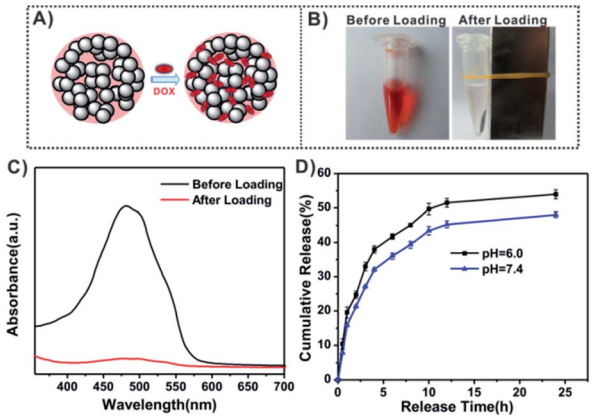

Fig. 2 (A) Schematic of the DOX loading process in porous Mn(0.25)-Fe_3O_4-III NPs. (B) Photographs of the DOX solution before and after incubation with porous Mn(0.25)-Fe_3O_4-III NPs. (C) UV-vis absorption spectra of the DOX solution before and after incubation with porous Mn(0.25)-Fe_3O_4-III NPs. (D) DOX release profiles from DOX/Mn(0.25)-Fe_3O_4-III NPs at pH 6.0 and pH 7.4 at 37 °C.

Mn(0.25)-Fe_3O_4-III NPs react as catalase in neutral conditions, rather than peroxidase.

The classical Fenton reaction is a catalytic process to convert H_2O_2 into reactive radicals (Fig. S2A†), which are capable of killing cancer cells, in the presence of Fe^{2+} or Fe^{3+} ions. Therefore, the efficiency of the Fenton reaction-mediated cancer therapy is mainly dependent on the catalytic activities of the Fenton reagents. Various iron-based nanostructures have been developed for the Fenton cancer treatment. However, the Fenton reaction activities of most reported nanoparticles are not strong, which greatly limit their applications in cancer treatment. Importantly, it was observed that the Fenton reaction activities of these Mn-doped magnetic nanoparticles could be greatly improved by controlling the molar ratio of Mn/Fe. To compare their Fenton reaction activities, the steady-state catalytic kinetics was studied in a reaction system containing magnetic nanoparticles (20 mg mL^{-1}), TMB and H_2O_2 of different concentrations (5, 12.5, 25, 50 and 100 mM) in HAc–NaAc buffer (pH = 4.8).

First, the time-dependent oxTMB concentration changes upon the addition of H_2O_2 were monitored (Fig. 4A and D). The absorbance changes were transformed to oxTMB concentration changes *via* the Beer–Lambert eqn (1), and the corresponding initial velocities (v_0) were calculated in the first three minutes. Then, the initial velocity (v_0) was plotted against corresponding H_2O_2 concentrations, followed by Michaelis–Menten eqn (2). Finally, through the formula deformation, the original Michaelis–Menten eqn (2) could be converted to be eqn (3). These equations are as follows:

$$A = \varepsilon bc \quad (1)$$

where A is the absorbance of oxTMB, ε ($\varepsilon = 3.9 \times 10^4\ M^{-1}\ cm^{-1}$) is the molar absorbance coefficient of oxTMB, b is the path length, and c is the molar concentration of oxTMB.

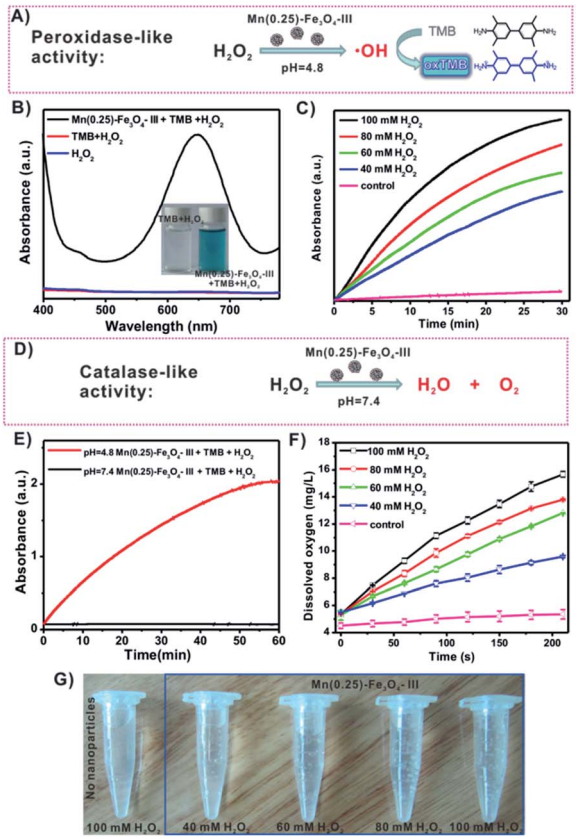

Fig. 3 *In vitro* characterizations of peroxidase-like catalytic activities and catalase-like catalytic activities of the porous Mn(0.25)-Fe_3O_4-III NPs. (A) Schematic of the peroxidase-like catalytic process of the porous Mn(0.25)-Fe_3O_4-III NPs. (B) Vis absorption spectra of the HAc–NaAc buffer (pH = 4.8) containing TMB and H_2O_2 catalysed by the porous Mn(0.25)-Fe_3O_4-III NPs. Inset shows the corresponding photographs of color reactions after 30 min incubation. (C) Vis absorption-time course curves of the TMB–H_2O_2 reaction system catalyzed by the porous Mn(0.25)-Fe_3O_4-III NPs in the HAc–NaAc buffer (pH = 4.8) (control group without magnetic NPs: TMB + 100 mM H_2O_2). (D) Schematic of the catalase-like catalytic process of the porous Mn(0.25)-Fe_3O_4-III NPs. (E) Vis absorption-time course curves of the TMB–H_2O_2 reaction system catalyzed by the porous Mn(0.25)-Fe_3O_4-III NPs in HAc–NaAc buffer (pH = 4.8) or PBS buffer (pH 7.4). (F) Dissolved oxygen time course curves of H_2O_2 catalyzed by the porous Mn(0.25)-Fe_3O_4-III NPs in PBS buffer (pH = 7.4) (control group without magnetic NPs: 100 mM H_2O_2). (G) Photographs of bubble reactions catalyzed by the porous Mn(0.25)-Fe_3O_4-III NPs after 6 h incubation.

$$v_0 = \frac{V_{max}[S]}{K_m + [S]} \quad (2)$$

$$\frac{1}{v_0} = \frac{K_m}{V_{max}[S]} + \frac{1}{V_{max}} \quad (3)$$

where v_0 is the initial velocity of the reaction, V_{max} is the maximal velocity of the reaction, $[S]$ is the substrate concentration and K_m is the Michaelis–Menten constant. According to the eqn (2), the Michaelis–Menten constant (K_m) and maximum velocity (V_{max}) were determined by the Lineweaver–Burk plot (Fig. 4B, C, E and F). Table 1 summarizes the kinetic parameters of these magnetic nanoparticles with different Mn doping. As

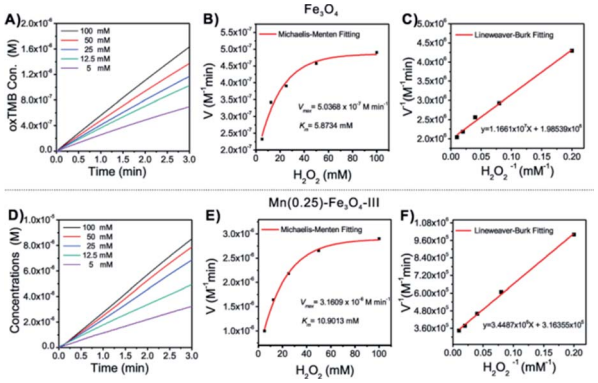

Fig. 4 Linear fitting of the concentration of oxTMB against time in the first 3 min for Fe_3O_4 NPs (A) and Mn(0.25)-Fe_3O_4-III NPs (D). The slope is used to calculate initial velocities. Michaelis–Menten kinetics (B and E) and Lineweaver–Burk plotting (C and F) for Fe_3O_4 NPs and Mn(0.25)-Fe_3O_4-III NPs with H_2O_2 as the substrate.

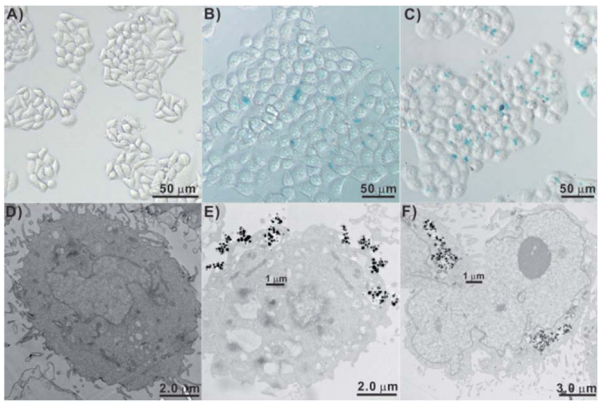

Fig. 5 (A)–(C) Micrographs of Prussian blue-stained HepG2 cells in the present or absent of the porous Mn(0.25)-Fe_3O_4-III NPs. Mn(0.25)-Fe_3O_4-III NPs were stained into blue: (A) 0 ppm (control group), (B) 5 ppm and (C) 10 ppm. (D) TEM image of HepG2 cells (control group). (E)–(F) TEM images showing cellular endocytic process of the Mn(0.25)-Fe_3O_4-III NPs (black dots) by HepG2 cells.

shown, by increasing the Mn doping level (x) of $(Mn_\chi Fe_{1-\chi})Fe_2O_4$ NPs from $\chi = 0$, to 0.14, 0.21, 0.25 and 0.30 (the chemical composition of the products were identified by inductively coupled plasma-atomic emission spectrophotometry (ICP-AES)), both V_{max} and K_m can be modulated. These results suggested that the affinity of Mn-doped Fe_3O_4 NPs towards H_2O_2 was slightly lower than that of pure porous Fe_3O_4 NPs, but the Mn-doped Fe_3O_4 NPs greatly increased the reaction rate. Meaningfully, the Mn(0.25)-Fe_3O_4-III NPs (the chemical composition is $(Mn_{0.25}Fe_{0.75})Fe_2O_4$) exhibited the highest Fenton reaction activities in comparison with other magnetic nanoparticles under the same conditions,[10,45,46] making them suitable for great potential application in cancer ferroptosis therapy. The improvement of Fenton reaction activities in our Mn-doped Fe_3O_4 nanosystem might be attributed to the small particle sizes and the synergetic catalysis effect of iron and manganese ions (Fig. S2 and S3†).

2.4 Internalization of Mn(0.25)-Fe_3O_4-III NPs in cancer cells

The internalization performance of the Mn(0.25)-Fe_3O_4-III NPs was further investigated by both Prussian blue staining method and TEM. It can be seen from Fig. 5A–C that the control HepG2 cells did not stain with the Prussian blue. However, the cells incubation with Mn(0.25)-Fe_3O_4-III NPs stained as blue color and the blue spots on the cells increased with the doses, indicating that these Mn(0.25)-Fe_3O_4-III NPs have entered into HepG2 cells. Furthermore, the TEM images of HepG2 cells treated with Mn(0.25)-Fe_3O_4-III NPs also proved that Mn(0.25)-Fe_3O_4-III NPs could penetrate the cellular membrane and accumulate in the protoplasm (Fig. 5E and F).

2.5 *In vitro* cytotoxicity of Mn(0.25)-Fe_3O_4-III NPs and anticancer therapy

The *in vitro* cytotoxicity of blank Mn(0.25)-Fe_3O_4-III NPs, free DOX and DOX/Mn(0.25)-Fe_3O_4-III NPs was evaluated against HepG2 cells by the MTT assay. As illustrated in Fig. 6A, no noticeable cytotoxicity was detected after 24 h co-incubation with blank Mn(0.25)-Fe_3O_4-III NPs. As the concentration of Mn(0.25)-Fe_3O_4-III NPs was up to 400 μg mL^{-1}, the cell viability could be maintained about 91%, indicating the excellent biocompatibility of the Mn(0.25)-Fe_3O_4-III NPs. As shown in Fig. 6B, it can be seen that the cytotoxicity of DOX/Mn(0.25)-Fe_3O_4-III NPs is higher than that of the free DOX under all tested concentrations. After incubation with DOX/Mn(0.25)-Fe_3O_4-III NPs and free DOX, the cell viabilities were ~49% and ~72% at the concentration of 5 μg mL^{-1}, ~36% and ~61% at the concentration of 10 μg mL^{-1}, and ~34% and ~58% at the concentration of 12.5 μg mL^{-1}, respectively.

Next, we investigated whether therapeutic efficacy could be improved by the combination of chemotherapy and ferroptosis therapy in our nanosystem. First, the concentration of H_2O_2 using in our *in vitro* treatment was optimized. No obvious

Table 1 The kinetic parameters of the magnetic nanoparticles with varied Mn doping. V_{max} is the maximal reaction velocity, K_m is the Michaelis constant and K_{cat} is the catalytic constant, where $K_{cat} = V_{max}/[C]$. The particle sizes of these samples were determined by SEM in Fig. S2

Samples (porous nanoparticles)	Nanoparticles concentration (C) (total metal ions, M)	Nanoparticles sizes (nm)	V_{max} (M min^{-1})	K_m (mM)	K_{cat} (min^{-1})
Fe_3O_4	2.5862×10^{-4}	~328	5.0368×10^{-7}	5.8734	1.9476×10^{-3}
$(Mn_{0.14}Fe_{0.86})Fe_2O_4$	2.5878×10^{-4}	~127	1.0862×10^{-6}	9.2336	4.1974×10^{-3}
$(Mn_{0.21}Fe_{0.79})Fe_2O_4$	2.5889×10^{-4}	~131	1.2327×10^{-6}	10.3341	4.7615×10^{-3}
$(Mn_{0.25}Fe_{0.75})Fe_2O_4$ [Mn(0.25)-Fe_3O_4-III]	2.5890×10^{-4}	~124	3.1609×10^{-6}	10.9013	1.2209×10^{-2}
$(Mn_{0.30}Fe_{0.70})Fe_2O_4$	2.5896×10^{-4}	~134	1.8406×10^{-6}	10.8552	7.1077×10^{-3}

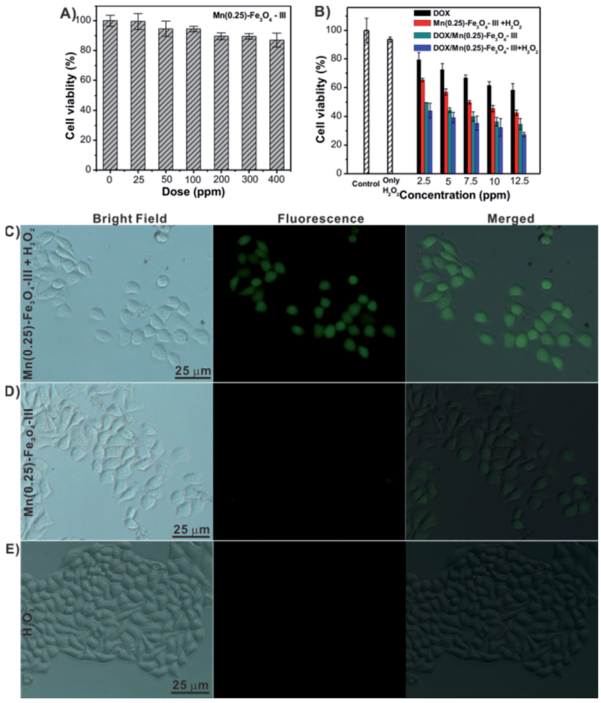

Fig. 6 (A) Relative viability of HepG2 cells incubated with the porous Mn(0.25)-Fe_3O_4-III NPs at different concentrations (0, 25, 50, 100, 200, 300 and 400 ppm) for 24 h. (B) Relative viability of HepG2 cells treated with free DOX, Mn(0.25)-Fe_3O_4-III NPs + H_2O_2, DOX/Mn(0.25)-Fe_3O_4-III NPs and DOX/Mn(0.25)-Fe_3O_4-III NPs + H_2O_2 at different DOX concentrations. Fluorescence microscopic images of DCFH-DA stained HepG2 cells after incubated with (C) Mn(0.25)-Fe_3O_4-III NPs + H_2O_2, (D) Mn(0.25)-Fe_3O_4-III NPs and (E) H_2O_2. HepG2 cells were stained by the fluorescence probe DCFH-DA, which could be oxidized by intracellular $^{\bullet}OH$ to emit green fluorescence.

cytotoxicity was found upon the addition of H_2O_2 below 100 mM (Fig. S4†). The MTT assay showed that DOX/Mn(0.25)-Fe_3O_4-III NPs in combination with H_2O_2 could enhance cell death dramatically. For instance, at the concentration of 12.5 μg mL^{-1}, DOX/Mn(0.25)-Fe_3O_4-III NPs or Mn(0.25)-Fe_3O_4-III/H_2O_2 alone showed good growth inhibition on HepG2 cells with cell viability ~34% and ~42%, respectively, whereas a significant increase in the cell death occurred in the presence of DOX/Mn(0.25)-Fe_3O_4-III NPs and H_2O_2 with cell viability ~27% (Fig. 6B). It is noteworthy to mention that both H_2O_2 alone and Mn(0.25)-Fe_3O_4-III NPs alone would not result in an obvious decrease in the cell death under the tested concentrations. Therefore, the cytotoxicity is attributed to the intracellular Fenton reaction between H_2O_2 and Mn(0.25)-Fe_3O_4-III NPs. To clearly observe the cell viability, the dead cells were stained with Trypan Blue. As depicted in Fig. S5†, under the treatment of DOX/Mn(0.25)-Fe_3O_4-III NPs and H_2O_2 together, the number of dead cells dramatically increased than that in the treatment with H_2O_2 or Mn(0.25)-Fe_3O_4-III NPs alone. All the results suggested that the anti-tumor therapeutic efficacy can be significantly improved with the synergistic effects of chemo- and ferroptosis-therapy in our drug delivery nanosystem.

In order to directly observe the ferroptosis effect, a ROS-sensitive fluorescence probe 2′,7′-dichlorofluorescin diacetate (DCFH-DA), which could be oxidized by $^{\bullet}OH$ to generate 2′,7′-dichlorofluorescein (DCF) with strong green fluorescence, was applied to monitor cellular $^{\bullet}OH$. In the two control groups (H_2O_2 and Mn(0.25)-Fe_3O_4-III NPs, Fig. 6D and E), there were no DCF fluorescence for the H_2O_2 group and weak DCF fluorescence for the Mn(0.25)-Fe_3O_4-III NP group in HepG2 cells. However, a significant fluorescence signal of DCF was detected in the H_2O_2/Mn(0.25)-Fe_3O_4-III NP group (Fig. 6C). The DCF fluorescence of these groups were further monitored by flow cytometry (Fig. S6†), which demonstrates that Mn(0.25)-Fe_3O_4-III NPs could significantly elevate the intracellular $^{\bullet}OH$ content by the iron-mediated Fenton reaction.

2.6 MR imaging

As mentioned above, the Mn(0.25)-Fe_3O_4-III NPs displayed an excellent biocompatibility and high saturation magnetization. Such important features of the Mn(0.25)-Fe_3O_4-III NPs put us forward to study their MRI contrast capability both *in vitro* and *in vivo*. From Fig. 7, the Mn(0.25)-Fe_3O_4-III NPs showed clear concentration-dependent darkening effect on a 9.4 T MRI scanner under T_2-weighted MR imaging (Fig. 7A). The T_2 relaxivity (r_2) was measured to be 181.2 mM S^{-1}. For *in vivo* MR imaging, HepG2 tumor-bearing mice were injected with the Mn(0.25)-Fe_3O_4-III NPs and then imaged (Fig. 7C and D). An obvious darkening effect could be observed in the tumor area at 2 h post injection, compared with 2 h post injection of PBS, indicating the outstanding T_2-weighted imaging performance of the Mn(0.25)-Fe_3O_4-III NPs *in vivo*.

2.7 *In vivo* anticancer therapy and biosafety

Finally, we further evaluated the *in vivo* treatment of the tumors in female BALB/c nude mice bearing subcutaneously injected with HepG2 cells on the right flank. After the tumors formation to

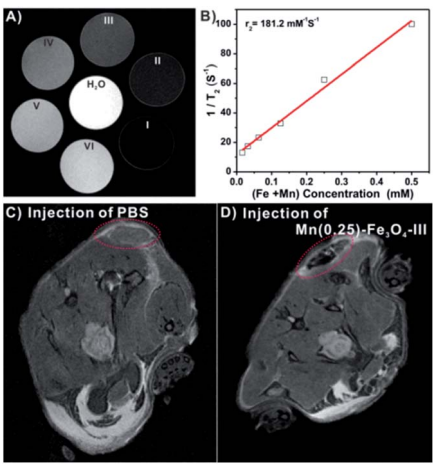

Fig. 7 *In vitro* and *in vivo* imaging analysis. (A) T_2-weighted MRI photograph of Mn(0.25)-Fe_3O_4-III NPs at different concentrations of total metal ions (Fe + Mn): (I) 0.5 mM; (II) 0.25 mM; (III) 0.125 mM; (IV) 0.0625 mM; (V) 0.03125 mM; (VI) 0.015625 mM. (B) Plots of $1/T_2$ against concentrations of total metal ions (Fe + Mn). (C) and (D) *In vivo* T_2-weighted MR images of the tumor-bearing mouse injection of PBS and Mn(0.25)-Fe_3O_4-III NPs (the red circles point to the tumor site).

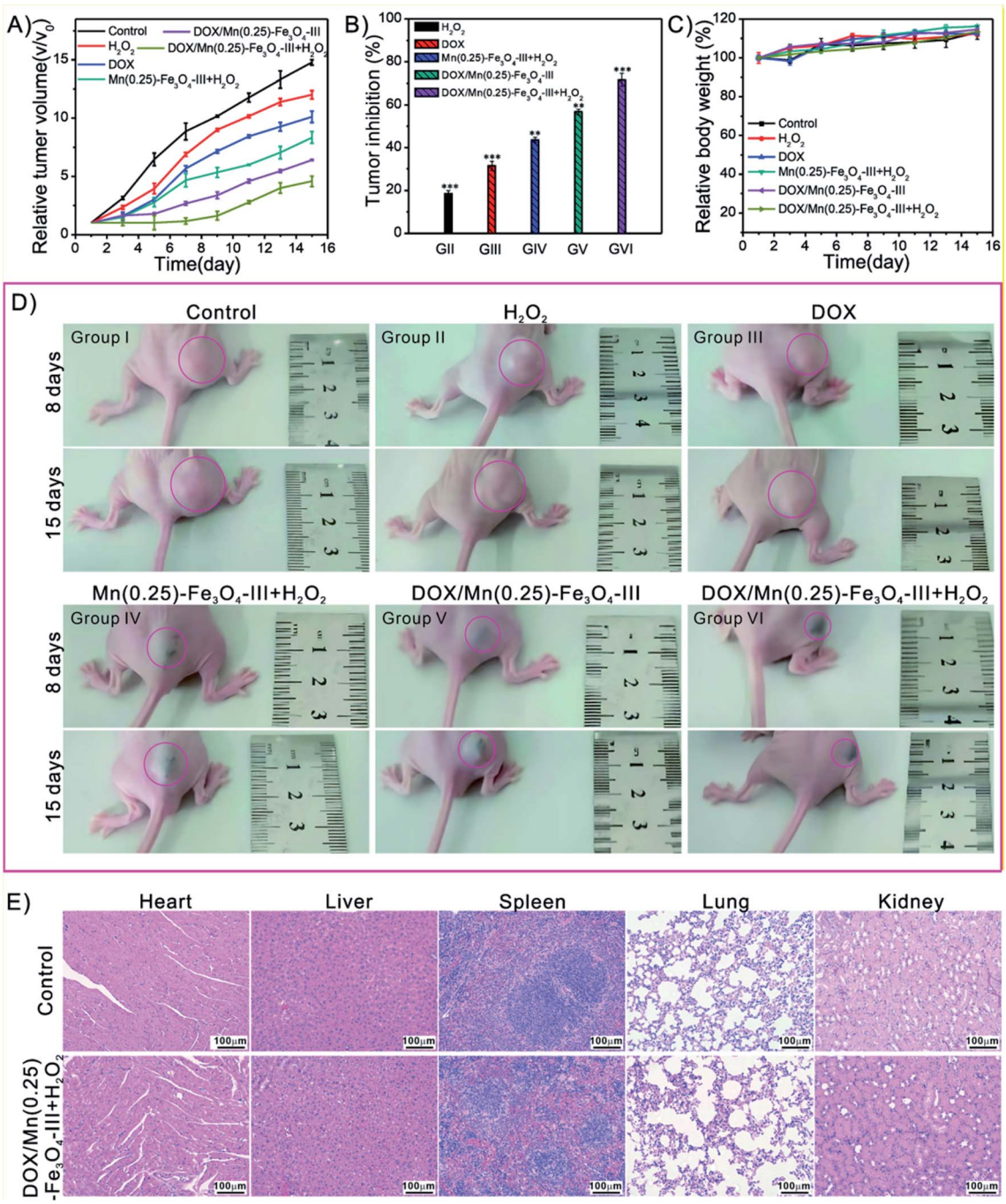

Fig. 8 (A) Relative tumor volumes of each group after different treatments. (B) Tumor inhibition ratios of mice after 15 days different treatments. $^{**}P$ <0.01, $^{***}P$ <0.001 *versus* the control experiments (Group I). (C) Relative body weight changes of each group after different treatments. (D) Representative photos of the tumor-bearing mice treated by six groups after 8 days and 15 days (the red circles point to the tumor site). (E) H&E staining images of major organs after 15 days different treatments.

50–60 mm^3, the mice were randomly divided into six groups for the 15 days observation: group I: PBS (control group), group II: H_2O_2, group III: free DOX, group IV: Mn(0.25)-Fe_3O_4-III NPs + H_2O_2, group V: DOX/Mn(0.25)-Fe_3O_4-III NPs, group VI: DOX/Mn(0.25)-Fe_3O_4-III NPs + H_2O_2. The drug and drug-loaded nanoparticles were injected into each mouse (dose = 10 mg kg^{-1} for DOX or an equivalent dose of DOX loaded into nanoparticles, please see experimental section for details). The relative tumor volumes and inhibition ratios of various treatments are summarized in Fig. 7A and B. It was found that the combination treatment group (group VI: DOX/Mn(0.25)-Fe_3O_4-III NPs + H_2O_2) exhibited very potent inhibition of tumor growth with the tumor inhibition ratio up to 71.6%. In comparison, the tumor growth was just partially inhibited by the other three groups (except control PBS group and H_2O_2 group) with tumor inhibition ratios only up to 31.5% for group III, 43.6% for group IV and 56.7% for

group V, respectively. After 8- and 15-day various treatments, the representative images of the tumor-bearing mice of each group are presented in Fig. 8D. It is clear to see that the group VI (DOX/Mn(0.25)-Fe_3O_4-III NPs + H_2O_2) has the smallest volume of tumors than the other five groups. Above all, the synergistic effect of combining chemotherapy and ferroptosis therapy can be discovered by the animal experiments.

In addition, there was a slightly increasing trend in body weights during the 15 days treatment (Fig. 8C). Moreover, no pathological changes were observed in the Hematoxylin and Eosin (H&E) staining of main organs including heart, liver, spleen, lung and kidney (Fig. 8E), demonstrating the biosafety of our nanocarrier system.

3. Conclusions

In conclusion, we have reported a facile one-pot route for the synthesis of magnetic Mn(0.25)-Fe_3O_4-III NPs with controllable porous structures, whole particle sizes and nanocrystal sizes. The obtained DOX/Mn(0.25)-Fe_3O_4-III NPs not only exhibited high Fenton reaction activity compared with the porous Fe_3O_4 NPs and many reported iron-based nanoparticles, but also could serve as a good T_2 contrast agent for MR imaging. Hence, such a nanosystem, with facile synthesis, good biocompatibility, excellent synergistic anticancer activity of chemotherapy and ferroptosis therapy and effective MR imaging, is promising for the future application of cancer treatment.

Ethical statement

All animal experiments operations were performed in accordance with the guidelines of the Institutional Animal Care and Use Committee (IACUC) and the care regulations approved by the Administrative Committee of Laboratory Animals of Anhui Medical University (No. LLSC20210778).

Author contributions

Designed the experiments: Weijun Fang and Tingting Zhao. Performed the experiments: Jianxiang Xu, Hanyuan Zhang, Yifeng Zhang and Xu Zhang. Analyzed the data: Weijun Fang, Jianxiang Xu, Hanyuan Zhang, Teng Wang and Shi Hong. Contributed to the writing of the manuscript: Weijun Fang, Tingting Zhao, Jianxiang Xu and Wenmei Wei. Revised to manuscript: Weijun Fang, Tingting Zhao and Wenmei Wei. All authors reviewed the manuscript.

Conflicts of interest

The authors declare that they have no known competing financial interests or personal relationships that could have appeared to influence the work reported in this paper.

Acknowledgements

We thank the National Natural Science Foundation of China (No. 21703255), the Natural Science Foundation of Anhui Province (No. 1908085MB47, 1708085MB35), the Key Projects of Anhui Province University Outstanding Youth Talent Support Program (No. gxyqZD2018021) and the Anhui Province Overseas Students Innovation Project Selection Funding Program-Key Project (No. 2021LCX003) for the financial support.

References

1 M. Colombo, S. Carregal-Romero, M. F. Casula, L. Gutierrez, M. P. Morales, I. B. Bohm, J. T. Heverhagen, D. Prosperi and W. J. Parak, Biological applications of magnetic nanoparticles, *Chem. Soc. Rev.*, 2012, **41**(11), 4306–4334.
2 A. Farzin, S. A. Etesami, J. Quint, A. Memic and A. Tamayol, Magnetic nanoparticles in cancer therapy and diagnosis, *Adv. Healthcare Mater.*, 2020, **9**(9), 1901058.
3 S. Z. Zhao, X. J. Yu, Y. N. Qian, W. Chen and J. L. Shen, Multifunctional magnetic iron oxide nanoparticles: an advanced platform for cancer theranostics, *Theranostics*, 2020, **10**(14), 6278–6309.
4 A. Singh and S. K. Sahoo, Magnetic nanoparticles: a novel platform for cancer theranostics, *Drug Discovery Today*, 2014, **19**(4), 474–481.
5 Y. X. J. Wang, Superparamagnetic iron oxide based MRI contrast agents: Current status of clinical application, *Quant. Imag. Med. Surg.*, 2011, **1**(1), 35–40.
6 J. Liu, S. Z. Qiao, Q. H. Hu and G. Q. Lu, Magnetic nanocomposites with mesoporous structures: Synthesis and applications, *Small*, 2011, **7**(4), 425–443.
7 S. Y. Yin, G. S. Song, Y. Yang, Y. Zhao, P. Wang, L. M. Zhu, X. Yin and X. B. Zhang, Persistent regulation of tumor microenvironment via circulating catalysis of $MnFe_2O_4$@metal-organic frameworks for enhanced photodynamic therapy, *Adv. Funct. Mater.*, 2019, **29**(25), 1901417.
8 A. Shah, M. S. Malik, G. S. Khan, E. Nosheen, F. J. Iftikhar, F. A. Khan, S. S. Shukla, M. S. Akhter, H. B. Kraatz and T. M. Aminabhavi, Stimuli-responsive peptide-based biomaterials as drug delivery systems, *Chem. Eng. J.*, 2018, **353**, 559–583.
9 P. A. Ma, H. H. Xiao, C. Yu, J. H. Liu, Z. Y. Cheng, H. Q. Song, X. Y. Zhang, C. X. Li, J. Q. Wang, Z. Gu and J. Lin, Enhanced cisplatin chemotherapy by iron oxide nanocarrier-mediated generation of highly toxic reactive oxygen species, *Nano Lett.*, 2017, **17**(2), 928–937.
10 M. F. Huo, L. Y. Wang, Y. Chen and J. L. Shi, Tumor-selective catalytic nanomedicine by nanocatalyst delivery, *Nat. Commun.*, 2017, **8**(1), 357.
11 G. Huang, H. B. Chen, Y. Dong, X. Q. Luo, H. J. Yu, Z. Moore, E. A. Bey, D. A. Boothman and J. M. Gao, Superparamagnetic iron oxide nanoparticles: amplifying ROS stress to improve anticancer drug efficacy, *Theranostics*, 2013, **3**(2), 116–126.
12 Q. An, C. Y. Sun, D. Li, K. Xu, J. Guo and C. C. Wang, Peroxidase-like activity of Fe_3O_4@carbon nanoparticles enhances ascorbic acid-induced oxidative stress and selective damage to PC-3 prostate cancer cells, *ACS Appl. Mater. Interfaces*, 2013, **5**(24), 13248–13257.

13 K. Sun, Z. G. Gao, Y. Zhang, H. S. Wu, C. Q. You, S. L. Wang, P. J. An, C. Sun and B. W. Sun, Enhanced highly toxic reactive oxygen species levels from iron oxide core-shell mesoporous silica nanocarrier-mediated fenton reactions for cancer therapy, *J. Mater. Chem. B*, 2018, **6**(37), 5876–5887.

14 M. J. Xuan, J. X. Shao, J. Zhao, Q. Li, L. R. Dai and J. B. Li, Magnetic mesoporous silica nanoparticles cloaked by red blood cell membranes: applications in cancer therapy, *Angew. Chem., Int. Ed.*, 2018, **57**(21), 6049–6053.

15 D. Q. Li, J. L. Ren, J. Li, Y. M. Zhang, Y. C. Lou, J. J. Zhu, P. Liu, Y. Chen, Z. Yu, L. Zhao, L. B. Zhang, X. Chen, J. T. Zhu and J. Tao, Ferroptosis-apoptosis combined anti-melanoma immunotherapy with a NIR-responsive upconverting $mSiO_2$ photodynamic platform, *Chem. Eng. J.*, 2021, **419**, 129557.

16 H. Liang, J. R. Guo, Y. Y. Shi, G. Z. Zhao, S. H. Sun and X. L. Sun, Porous yolk-shell Fe/Fe_3O_4 nanoparticles with controlled exposure of highly active Fe(0) for cancer therapy, *Biomaterials*, 2021, **268**, 120530.

17 G. B. Yang, H. Gong, T. Liu, X. Q. Sun, L. Cheng and Z. Liu, Two-dimensional magnetic $WS_2@Fe_3O_4$ nanocomposite with mesoporous silica coating for drug delivery and imaging-guided therapy of cancer, *Biomaterials*, 2015, **60**, 62–71.

18 Y. Chao, G. B. Chen, C. Liang, J. Xu, Z. L. Dong, X. Han, C. Wang and Z. Liu, Iron nanoparticles for low-power local magnetic hyperthermia in combination with immune checkpoint blockade for systemic antitumor therapy, *Nano Lett.*, 2019, **19**(7), 4287–4296.

19 S. J. Dixon, K. M. Lemberg, M. R. Lamprecht, R. Skouta, E. M. Zaitsev, C. E. Gleason, D. N. Patel, A. J. Bauer, A. M. Cantley, W. S. Yang, B. Morrison and B. R. Stockwell, Ferroptosis: an iron-dependent form of nonapoptotic cell death, *Cell*, 2012, **149**(5), 1060–1072.

20 Z. Y. Shen, J. B. Song, B. C. Yung, Z. J. Zhou, A. G. Wu and X. Y. Chen, Emerging strategies of cancer therapy based on ferroptosis, *Adv. Mater.*, 2018, **30**(12), 1704007.

21 S. Doll and M. Conrad, Iron and ferroptosis: a still ill-defined liaison, *IUBMB Life*, 2017, **69**(6), 423–434.

22 J. P. F. Angeli, M. Schneider, B. Proneth, Y. Y. Tyurina, V. A. Tyurin, V. J. Hammond, N. Herbach, M. Aichler, A. Walch, E. Eggenhofer, D. Basavarajappa, O. Radmark, S. Kobayashi, T. Seibt, H. Beck, F. Neff, I. Esposito, R. Wanke, H. Forster, O. Yefremova, M. Heinrichmeyer, G. W. Bornkamm, E. K. Geissler, S. B. Thomas, B. R. Stockwell, V. B. O'Donnell, V. E. Kagan, J. A. Schick and M. Conrad, Inactivation of the ferroptosis regulator Gpx_4 triggers acute renal failure in mice, *Nat. Cell Biol.*, 2014, **16**(12), 1180–1191.

23 N. Yagoda, M. von Rechenberg, E. Zaganjor, A. J. Bauer, W. S. Yang, D. J. Fridman, A. J. Wolpaw, I. Smukste, J. M. Peltier, J. J. Boniface, R. Smith, S. L. Lessnick, S. Sahasrabudhe and B. R. Stockwell, RAS-RAF-MEK-dependent oxidative cell death involving voltage-dependent anion channels, *Nature*, 2007, **447**(7146), 864–868.

24 S. J. Dixon and B. R. Stockwell, The role of iron and reactive oxygen species in cell death, *Nat. Chem. Biol.*, 2014, **10**(1), 9–17.

25 J. Y. Cao and S. J. Dixon, Mechanisms of ferroptosis, *Cell. Mol. Life Sci.*, 2016, **73**(11–12), 2195–2209.

26 Z. Y. Shen, T. Liu, Y. Li, J. Lau, Z. Yang, W. P. Fan, Z. J. Zhou, C. R. Shi, C. Ke, V. I. Bregadze, S. K. Mandal, Y. J. Liu, Z. H. Li, T. Xue, G. Z. Zhu, J. Munasinghe, G. Niu, A. G. Wu and X. Y. Chen, Fenton-reaction-acceleratable magnetic nanoparticles for ferroptosis therapy of orthotopic brain tumors, *ACS Nano*, 2018, **12**(11), 11355–11365.

27 H. Ranji-Burachaloo, P. A. Gurr, D. E. Dunstan and G. G. Qiao, Cancer treatment through nanoparticle-facilitated fenton reaction, *ACS Nano*, 2018, **12**(12), 11819–11837.

28 C. Liang, X. L. Zhang, M. S. Yang and X. C. Dong, Recent progress in ferroptosis inducers for cancer therapy, *Adv. Mater.*, 2019, **31**(51), 1904197.

29 X. Z. Shan, S. M. Li, B. J. Sun, Q. Chen, J. Sun, Z. G. He and C. Luo, Ferroptosis-driven nanotherapeutics for cancer treatment, *J. Controlled Release*, 2020, **319**, 322–332.

30 L. Z. Gao, J. Zhuang, L. Nie, J. B. Zhang, Y. Zhang, N. Gu, T. H. Wang, J. Feng, D. L. Yang, S. Perrett and X. Yan, Intrinsic peroxidase-like activity of ferromagnetic nanoparticles, *Nat. Nanotechnol.*, 2008, **2**(9), 577–583.

31 Z. L. Gao, T. He, P. Y. Zhang, X. Y. Li, Y. L. Zhang, J. Lin, J. C. Hao, P. Huang and J. W. Cui, Polypeptide-based theranostics with tumor-microenvironment- activatable cascade reaction for chemo-ferroptosis combination therapy, *ACS Appl. Mater. Interfaces*, 2020, **12**(18), 20271–20280.

32 Q. Jiang, K. Wang, X. Y. Zhang, B. S. Ouyang, H. X. Liu, Z. Q. Pang and W. L. Yang, Platelet membrane-camouflaged magnetic nanoparticles for ferroptosis-enhanced cancer immunotherapy, *Small*, 2020, **16**(22), 2001704.

33 Q. F. Chen, X. B. Ma, L. Xie, W. J. Chen, Z. G. Xu, E. Q. Song, X. K. Zhu and Y. Song, Iron-based nanoparticles for MR imaging-guided ferroptosis in combination with photodynamic therapy to enhance cancer treatment, *Nanoscale*, 2021, **13**(9), 4855–4870.

34 Y. C. Yang, Q. Tian, S. Q. Wu, Y. X. Li, K. Yang, Y. Yan, L. Shang, A. P. Li and L. B. Zhang, Blue light-triggered Fe^{2+}-release from monodispersed ferrihydrite nanoparticles for cancer iron therapy, *Biomaterials*, 2021, **271**, 120739.

35 Z. W. Chen, J. J. Yin, Y. T. Zhou, Y. Zhang, L. Song, M. J. Song, S. L. Hu and N. Gu, Dual enzyme-like activities of iron oxide nanoparticles and their implication for diminishing cytotoxicity, *ACS Nano*, 2012, **6**(5), 4001–4012.

36 L. D. Yue, J. L. Wang, Z. C. Dai, Z. F. Hu, X. Chen, Y. F. Qi, X. W. Zheng and D. X. Yu, pH-responsive, self-sacrificial nanotheranostic agent for potential in vivo and in vitro dual modal MRI/CT imaging, real-time, and in situ monitoring of cancer therapy, *Bioconjugate Chem.*, 2017, **28**(2), 400–409.

37 Q. Q. Liu, K. K. Du, M. Liu, R. Lv, B. W. Sun, D. W. Cao, N. Y. He and Z. F. Wang, Sulfosalicylic acid/Fe^{3+} based nanoscale coordination polymers for effective cancer therapy by the fenton reaction: an inspiration for

understanding the role of aspirin in the prevention of cancer, *Biomater. Sci.*, 2019, **7**(12), 5482–5491.

38 T. Liu, W. L. Liu, M. K. Zhang, W. Y. Yu, F. Gao, C. X. Li, S. B. Wang, J. Feng and X. Z. Zhang, Ferrous-supply-regeneration nanoengineering for cancer-cell-specific ferroptosis in combination with imaging-guided photodynamic therapy, *ACS Nano*, 2018, **12**(12), 12181–12192.

39 Z. H. Guo, W. S. Xie, J. S. Lu, X. X. Guo, Y. J. Chi, D. Wang, N. Takuya, W. L. Xu, J. L. Ye, X. Y. Liu, Z. Gu, B. H. Xu, H. Wu and L. Y. Zhao, Ferrous ions doped layered double hydroxide: smart 2D nanotheranostic platform with imaging-guided synergistic chemo/photothermal therapy for breast cancer, *Biomater. Sci.*, 2021, **9**(17), 5928–5938.

40 W. H. Yao, C. Y. Liu, N. Wang, H. J. Zhou, H. L. Chen and W. H. Qiao, Triple-responsive targeted hybrid liposomes with high MRI performance for tumor diagnosis and therapy, *Mater. Chem. Front.*, 2021, **5**(16), 6226–6243.

41 H. F. Sun, Z. H. Zhang, X. Y. Kang, Q. Dai, A. X. Song, J. C. Hao and J. W. Cui, Biologically-derived nanoparticles for chemo-ferroptosis combination therapy, *Mater. Chem. Front.*, 2021, **5**(10), 3813–3822.

42 B. W. Yang, L. Ding, H. L. Yao, Y. Chen and J. L. Shi, A metal-organic framework (MOF) fenton nanoagent-enabled nanocatalytic cancer therapy in synergy with autophagy inhibition, *Adv. Mater.*, 2020, **32**(12), 1907152.

43 D. W. Zheng, Q. Lei, J. Y. Zhu, J. X. Fan, C. X. Li, C. Li, Z. S. Xu, S. X. Cheng and X. Z. Zhang, Switching apoptosis to ferroptosis: metal-organic network for high-efficiency anticancer therapy, *Nano Lett.*, 2017, **17**(1), 284–291.

44 Y. Liu, W. Y. Zhen, L. H. Jin, S. T. Zhang, G. Y. Sun, T. Q. Zhang, X. Xu, S. Y. Song, Y. H. Wang, J. H. Liu and H. J. Zhang, All-in-one theranostic nanoagent with enhanced reactive oxygen species generation and modulating tumor microenvironment ability for effective tumor eradication, *ACS Nano*, 2018, **12**(5), 4886–4893.

45 Y. Du, C. Yang, F. Y. Li, H. W. Liao, Z. Chen, P. H. Lin, N. Wang, Y. Zhou, J. Y. Lee, Q. Ding and D. S. Ling, Core-shell-satellite nanomaces as remotely controlled self-fueling fenton reagents for imaging-guided triple-negative breast cancer-specific therapy, *Small*, 2020, **16**(31), 2002537.

46 S. S. Gao, H. Lin, H. X. Zhang, H. L. Yao, Y. Chen and J. L. Shi, Nanocatalytic tumor therapy by biomimetic dual inorganic nanozyme-catalyzed cascade reaction, *Adv. Sci.*, 2019, **6**(3), 1801733.

47 H. T. Bi, Y. L. Dai, P. P. Yang, J. T. Xu, D. Yang, S. L. Gai, F. He, B. Liu, C. N. Zhong, G. H. An and J. Lin, Glutathione mediated size-tunable UCNPs-Pt(IV)-$ZnFe_2O_4$ nanocomposite for multiple bioimaging guided synergetic therapy, *Small*, 2018, **14**(13), 1703809.

48 J. T. Jang, H. Nah, J. H. Lee, S. H. Moon, M. G. Kim and J. Cheon, Critical enhancements of MRI contrast and hyperthermic effects by dopant-controlled magnetic nanoparticles, *Angew. Chem., Int. Ed.*, 2009, **48**(7), 1234–1238.

49 J. H. Lee, Y. M. Huh, Y. Jun, J. Seo, J. Jang, H. T. Song, S. Kim, E. J. Cho, H. G. Yoon, J. S. Suh and J. Cheon, Artificially engineered magnetic nanoparticles for ultra-sensitive molecular imaging, *Nat. Med.*, 2007, **13**(1), 95–99.

50 W. Fang, W. Zhu, H. Chen, H. Zhang, S. Hong, W. Wei and T. Zhao, MRI enhancement and tumor targeted drug delivery using Zn^{2+}-doped Fe_3O_4 core/mesoporous silica shell nanocomposites, *ACS Appl. Bio Mater.*, 2020, **3**(3), 1690–1697.

51 A. D. Bokare and W. Choi, Review of iron-free fenton-like systems for activating H_2O_2 in advanced oxidation processes, *J. Hazard. Mater.*, 2014, **275**, 121–135.

52 Z. Z. Wang, Y. Zhang, E. G. Ju, Z. Liu, F. F. Cao, Z. W. Chen, J. S. Ren and X. G. Qu, Biomimetic nanoflowers by self-assembly of nanozymes to induce intracellular oxidative damage against hypoxic tumors, *Nat. Commun.*, 2018, **9**(1), 3334.

53 L. S. Lin, J. B. Song, L. Song, K. M. Ke, Y. J. Liu, Z. J. Zhou, Z. Y. Shen, J. Li, Z. Yang, W. Tang, G. Niu, H. H. Yang and X. Y. Chen, Simultaneous fenton-like ion delivery and glutathione depletion by MnO_2-based nanoagent to enhance chemodynamic therapy, *Angew. Chem., Int. Ed.*, 2018, **57**(18), 4902–4906.

54 D. Wu, X. H. Duan, Q. Q. Guan, J. Liu, X. Yang, F. Zhang, P. Huang, J. Shen, X. T. Shuai and Z. Cao, Mesoporous polydopamine carrying manganese carbonyl responds to tumor microenvironment for multimodal imaging-guided cancer therapy, *Adv. Funct. Mater.*, 2019, **29**(16), 1900095.